ORIGINAL ARTICLE

CrossMark

Development of a Single-Moment Cloud Microphysics Scheme with Prognostic Hail for the Weather Research and Forecasting (WRF) Model

Soo Ya Bae[1] · **Song-You Hong**[1] · **Wei-Kuo Tao**[2]

Abstract

This study examines the effect of hail on microphysical processes and precipitation. The Weather Research and Forecasting (WRF) Single-Moment 7-class Microphysics (WSM7) is developed by introducing the hail hydrometeor as an additional prognostic water substance within the WSM6 scheme, which are four-ice and three-ice schemes, respectively. In an idealized 2D squall case, the WSM7 scheme with hail tends to enhance the accretion rate of ice particles due to the faster sedimentation of hail than that of graupel in the WSM6 scheme. The amount of hail is largely compensated with the reduction of graupel, but its maximum at lower altitudes. Weakened accretion of graupel by snow at higher altitudes maintains the snow aloft, and increases of it at the mid-level. The reduced sum of graupel and hail at the melting level leads to a decrease in the mixing ratio of rain in the WSM7 experiment, which is compensated by falling hail. In 3D squall line experiments, the WSM7 scheme tends to enhance convective activities in the leading edge of the squall line, whereas the precipitation intensity in the trailing stratiform region decreases. This is due to the fact that the addition of hail plays a role in suppressing light precipitation and increasing heavy precipitation activities.

1 Introduction

Hong et al. (2004) suggested a revised approach for ice-microphysical processes to overcome the limitations identified in previous studies. Weather Research and Forecasting (WRF) Single-Moment-Microphysics schemes (WSMMPs) have been developed based on the study of Hong et al. (2004). WSMMPs have three categories: (1) 3-class (WSM3) with water vapor, cloud water/ice, and rain/snow; (2) 5-class (WSM5) with water, cloud water, cloud ice, rain, and snow; and (3) 6-class (WSM6) with graupel added to WSM5. As of January 2018, WSM6 is a three-ice microphys-ics scheme with an option to switch to 3ICE-graupel or 3ICE-hail. Among WSMMPs, the WSM6 scheme has been widely used for weather prediction.

Numerous reports have evaluated the performance of the scheme for various weather phenomena, including over the US (Grasso et al. 2014), a hurricane over the Atlantic (Li and Pu 2008), and heavy rainfall over East Asia (Lim and Hong 2005; Shin and Hong 2009). These studies demonstrate that the WSM6 scheme is a promising option for the WRF model because of its capability to reproduce precipitating convection and associated meteorological phenomena. However, some systematic deficien-cies, such as too much light precipitation activity (Shi et al. 2007) and an excessive amount of graupel compared to snow (Lin and Colle 2009), have been reported. A further revision to the WSM6 scheme using a combined sedimentation velocity for graupel and snow (Dudhia et al. 2008) helped alleviate the problem of exces-sive graupel, but this scheme has remained systematic problems, a wider area of light precipitation and lower heavy precipitation (Han et al. 2013).

Hailstorm is a major severe weather hazard in various part of the world. Severe hail can cause damage such as broken windows, dents in cars, damage to crops, and injury to humans

---

Responsible editor: Rokjin Park

✉ Soo Ya Bae
sy.bae@kiaps.org

[1] Korea Institute of Atmospheric Prediction Systems (KIAPS), 35 Boramae-ro 5-gil, Dongjak-gu, Seoul 07071, South Korea

[2] Mesoscale Atmospheric Processes Laboratory, NASA Goddard Space Flight Center, Greenbelt, MD 20771, USA

and livestock (Luo et al. 2017). Both hail and/or graupel can occur simultaneously in real weather events with cloud ice and snow. Therefore, a four-ice scheme (cloud ice, snow, graupel, and hail) is required to represent ice processes realistically. However, bulk microphysics schemes have traditionally represented ice particles by separating them into predefined categories below three-ice (ice, snow, and graupel; e.g. Colle and Zeng 2004; Hong et al. 2004; Morrison et al. 2005; Thompson et al. 2008; Lim and Hong 2010; Hong et al. 2010, and many others). Some schemes have an option to switch hail or graupel processes (3ICE-graupel or 3ICE-hail), but are supposed to have a limitation for simulating precipitation, reflectivity, and vertical distribution of squall line structure (Wu et al. 2013; Tao et al. 2016).

Recently, microphysics schemes with four-ice categories have been developed to improve the precipitation forecasting performance of mesoscale numerical models and cumulus cloud ensemble models (van Weverberg et al. 2012; Milbrandt and Morrison 2013; Lang et al. 2014). Tao et al. (2016) showed that the frequency of heavy precipitation simulated with a four-ice scheme is higher than that with a 3-ice scheme. They also found that the distribution of precipitation and reflectivity with a four-ice scheme is closer to observations. As of January 2018, four-ice microphysics schemes do not exist in the WRF model.

The purpose of this study is to examine the effect of hail on a single-moment bulk microphysics scheme by adding hail processes to the corresponding WSM6 scheme (Hong et al. 2004; Hong and Lim 2006). The new scheme is called the WRF single-moment 7-class (WSM7) microphysics scheme. Idealized simulations are often used to test new microphysics schemes because their behavior can be tested in a setting that is open to simpler interpretation. Therefore, an idealized 2D storm testbed is utilized to examine the fundamental characteristics of microphysical processes in relation to the hail species. A 3D real-case is selected to investigate the effect of hail-related microphysical processes on the simulated storm morphology.

The addition of hail to the WSM6 scheme is described in section 2, along with the model setup of the sensitivity experiments. The results are discussed in section 3. This paper ends with a summary and concluding remarks.

2 WSM7 Scheme and Experimental Setup

2.1 Major Components of WSM7

A schematic diagram of source/sink terms of the WSM7 scheme is shown in Fig. 1. Each source/sink term in Fig. 1 is defined in the Appendix, along with a list of symbols in Appendix Table 2. Additional terms related to hail are based on previous work by Lin et al. (1983), Rutledge and Hobbs (1984), and Lang et al. (2014).

The hail size distribution in the present scheme is assumed to follow the exponential form, which is represented as

$$n_H(D_H)\mathrm{d}D_H = n_{0H}exp(-\lambda_H D_H)\mathrm{d}D_H, \tag{1}$$

where $n_H(D_H)\mathrm{d}D_H$ is the number of hail particles per m^3 of air with diameters between D_H and $D_H + dD_H$ in m^{-4}, n_{0H} is the intercept parameter in m^{-4}, and λ_H is the slope of the distribution in m^{-1}. This slope is given by

$$\lambda_H = \left(\frac{\pi \rho_H n_{0H}}{\rho q_H}\right)^{0.25}, \tag{2}$$

where ρ_H is the density of hail in $\mathrm{kg\,m}^{-3}$, ρ is the density of air in $\mathrm{kg\,m}^{-3}$, and q_H is the mixing ratio of hail in $\mathrm{kg\,kg}^{-1}$. In this study, we assume that $n_{0H} = 4 \times 10^4\,\mathrm{m}^{-4}$ based on Lin et al. (1983).

The governing equation for hail is given by

$$\frac{\partial q_H}{\partial t} = -\mathrm{V} \cdot \nabla_3 q_H - \frac{q_H}{\rho}\frac{\partial}{\partial z}(\rho V_H) + S_H, \tag{3}$$

where the first and second terms on the right-hand side are the 3D advection and sedimentation of hail, respectively. S_H is the source and sink of hail. The mass-weighted mean terminal velocity can be obtained by integrating the terminal velocity of hail, which is expressed as

$$V_H = \frac{\int V_H(D_H)q_H(D_H)dD_H}{\int q_H(D_H)dD_H} = \frac{a_H}{\lambda_H^{b_H}}\Gamma(4 + b_H)\left(\frac{\rho_0}{\rho}\right)^{1/2}, \tag{4}$$

where the terminal velocity $V_H(D_H)$ for hail with diameter D_H is based on the equation determined by Locatelli and Hobbs (1974) and is expressed as

$$V_H(D_H) = a_H D_H^{b_H}\left(\frac{\rho_0}{\rho}\right)^{1/2}. \tag{5}$$

a_H and b_H are the empirical formula of V_H with values of 285 $\mathrm{m}^{1-b}{}_H\,\mathrm{s}^{-1}$ and 0.8 (unitless), respectively.

2.2 Model Setup

The Advanced Research WRF version 3.7.1 (ARW; Skamarock et al. 2008), which was released in August 2015, is used. Idealized experiments are designed to analyze the intrinsic differences between the WSM6 and WSM7 schemes systematically. The present study follows the experimental design of Morrison et al. (2009) and Lim and Hong (2010) that have evaluated the characteristics of the simulated storm with respect to the differences in microphysical processes. The grid in the x direction comprises 601 points with a 1-km grid spacing and there are 80 vertical
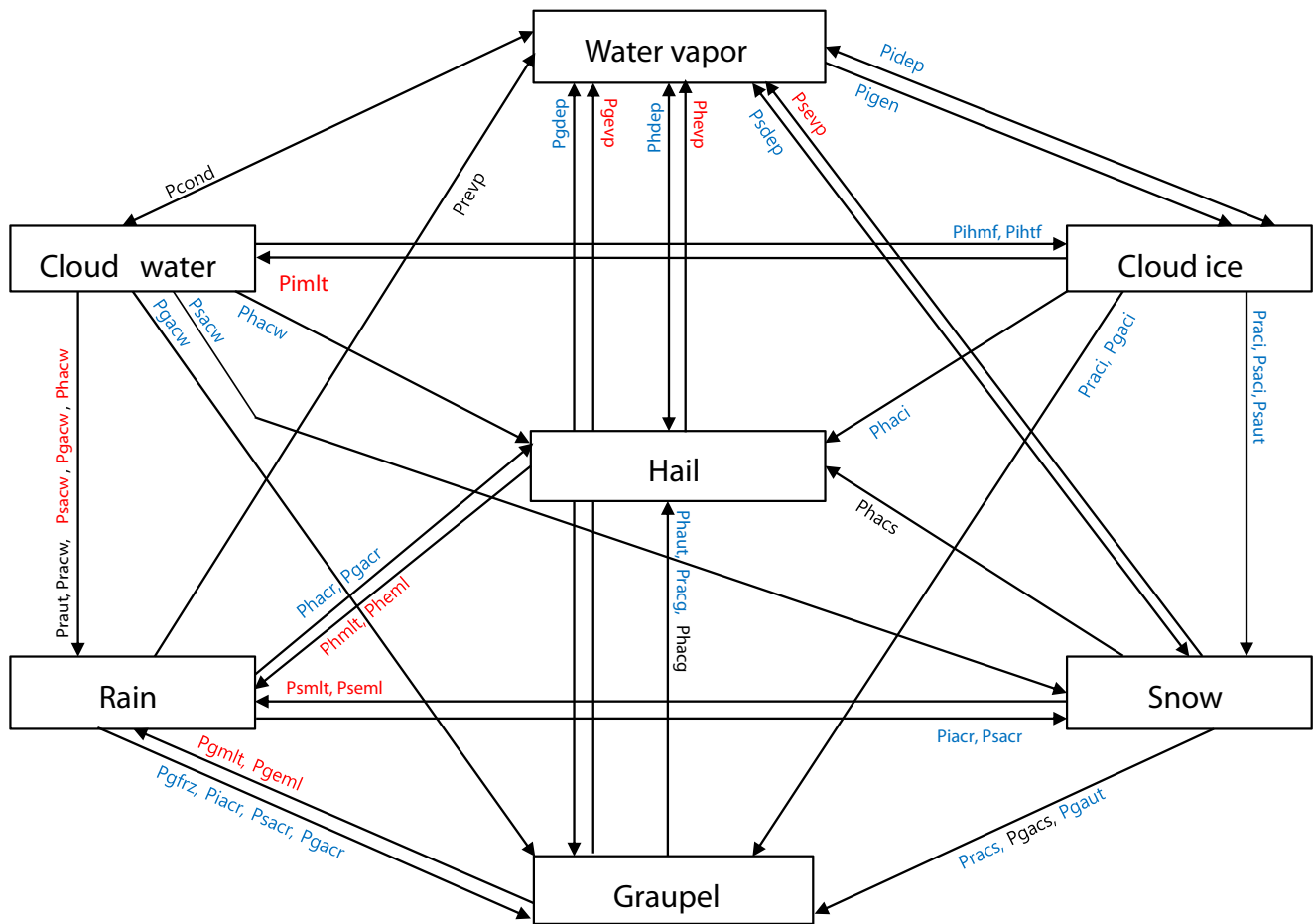
Fig. 1 Flowchart of the microphysical processes in the WSM7 scheme. The terms with red (blue) color are activated when the temperature is above (below) 0 °C, whereas the terms with black color are in the entire regime of temperature

layers. The model is integrated for 7 h with time steps of 5 s. The initial conditions include a warm bubble with a 4-km radius and a maximum perturbation of 3 K at the center of the domain. Wind with a velocity of 12 m s^{-1} is applied in the positive x direction at the surface; its velocity decreases to zero at 2.5 km above the ground with no wind above this level. Open boundary conditions are applied, and there was no Coriolis force or friction. The parameters for hail and graupel are presented in Table 1.

Real-case experiments are designed for the 20 May 2011 Midlatitude Continental Convective Clouds Experiment (MC3E) case. MC3E is a joint field campaign of the US Department of Energy's (DOE) Atmospheric Radiation Measurement Program Climate Research Facility and the NASA Global Precipitation Measurement (GPM) Mission Ground Validation Program (Petersen and Jensen 2012). On 20 May 2011, a deep, upper level low over the central Great Basin moved across the central and southern Rockies and into the central and northern Plains. The northern portion of a long convective line began to enter the MC3E sounding network on 07 UTC 20 May. By 09 UTC, it had merged with ongoing convection near the

Kansas–Oklahoma border to form a more intense convective segment with a well-defined trailing region (Tao et al. 2016; Lang et al. 2014).

Table 1 Parameters of the size distribution and terminal velocity in the sensitivity experiments

Hydrometeor Parameter	Snow	Graupel	Hail
n_0, m^{-4}	2×10^6	4×10^6	4×10^4
ρ, kg m^{-3}	100	500	912
λ_X^2, m^{-1}	890	1538	582
a	11.72	330	285.
b	0.41	0.8	0.8
$\overline{V}^a$, m s^{-1}	1.24	2.70	5.20

*n_0 is the intercept; ρ is the density; λ is the slope parameter as $\left(\frac{\pi \rho_X n_{0X}}{\rho_a q}\right)^{0.25}$; $\overline{V}$ is the mass-weighted mean terminal velocity as $\frac{a_X \Gamma(4+b_X)}{6} \frac{a_X \Gamma(4+b_X)}{6} \left(\frac{a_X \Gamma(4+b_X)}{6}\right)^{0.5}$

[a] The mixing ratio of graupel and hail is assumed to be 1.0 g kg^{-1}

The grid configuration includes an outer domain and two inner-nested domains with a horizontal grid spacing of 9, 3, and 1 km using 524 × 380, 673 × 442, and 790 × 535 grid points, respectively. The number of vertical level is 61, and the model top is located at 50 hPa. Time steps of 18, 6, and 2 s are used in these nested grids, respectively. The Grell-Devenyi cumulus parameterization scheme (Grell and Devenyi 2002) is used only for the outer grid (9 km). For the two inner domains (3 and 1 km), the convective scheme is turned off. The Goddard broadband two-stream (upward and downward fluxes) approach was used for the short- and long-wave radiative flux and atmospheric heating calculations (Chou and Suarez 1999, 2001). The planetary boundary layer parameterization employed the Mellor-Yamada-Janjic (Mellor and Yamada 1982) scheme. The detailed grid and physics information for these experiments are described

in Tao et al. (2016). Initial conditions are from the GFS-FNL (Global Forecast System Final global gridded analysis archive) on 1.0° × 1.0° grids, and the lateral boundary conditions are updated every 6 h.

3 Results

3.1 Idealized Squall-Line Simulation

Figure 2 presents Hovmöller plots of the surface rainfall rate and maximum vertical reflectivity. Reflectivity is calculated using a simulated equivalent reflectivity factor, which is defined as the sixth moment of the drop size distribution based on the available mixing ratios for the precipitation species
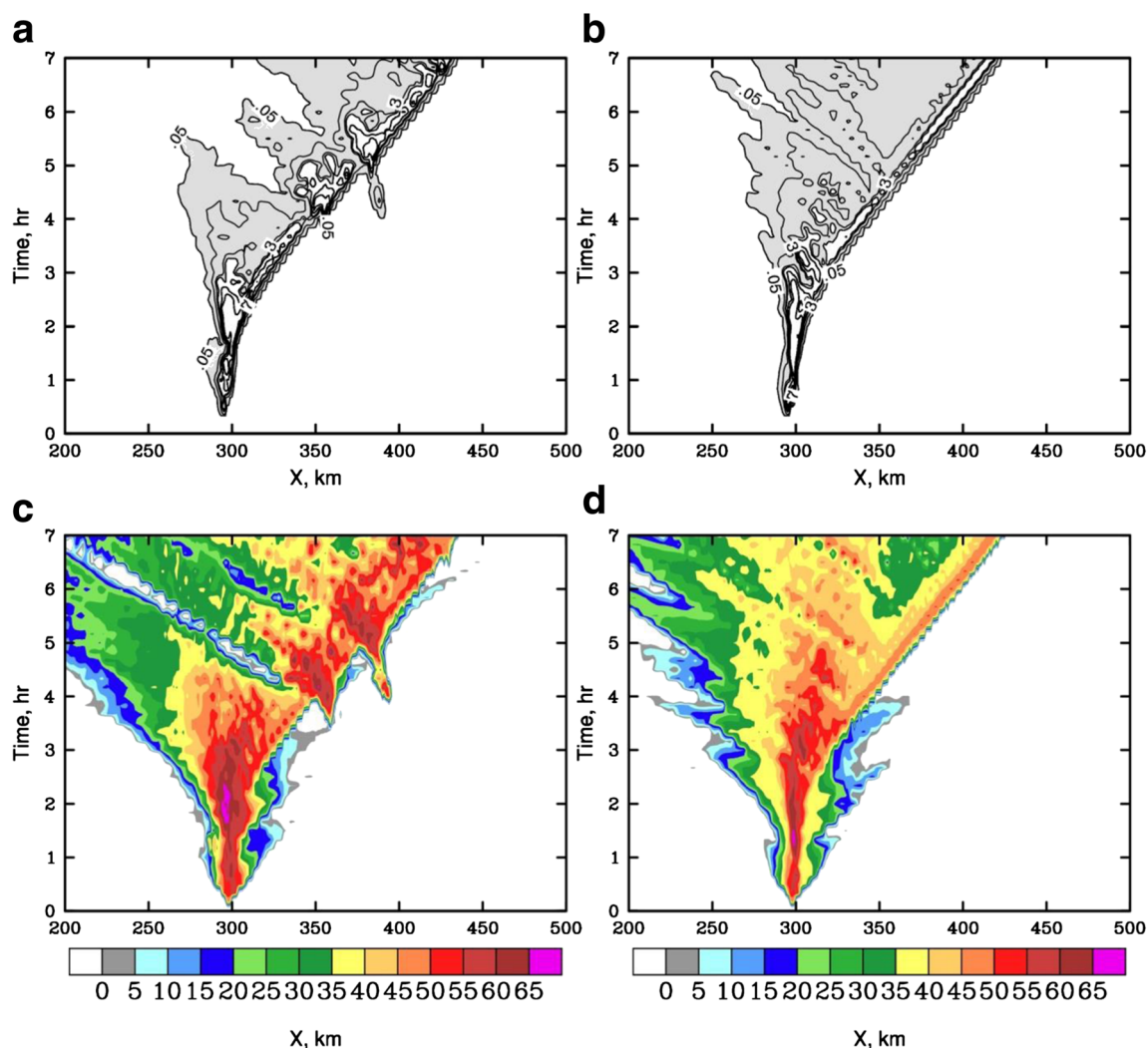

Fig. 2 Hovmöller plots of the surface rainfall rate for the (**a**) WSM6 and (**b**) WSM7 simulations. The contour interval is every 1 mm (10 min) for the rates of 0–4 mm (10 min) and every 3 mm (10 min) for the rates greater than 4 mm (10 min). To highlight the stratiform rain region, the precipitation rates of 0.05–4 mm (10 min) are shaded gray. **c**, **d** Maximum reflectivity from WSM 6 and WSM7, respectively

(rain, snow, graupel, and hail). The comparison of surface precipitation rate demonstrates a typical evolution of a storm associated with squall line development in both experiments (Fig. 2a, b). Compared to WSM6 (Fig. 2a), WSM7 (Fig. 2b) suppresses precipitation activities, especially along the leading edge. This characteristic is clearly seen in the evolution of reflectivity (Fig. 2c, d). Reflectivity in WSM6 has higher value at the front of the leading edge, where are at 350 km for 3.5 h and 4 h and at 400 km for 4 h and 5 h. The strong

reflectivity (> 50) area in WSM6 is broader than that in WSM7 but the moderate reflectivity (35 < reflectivity <45) area in WSM6 is narrower.

The maximum reflectivity of ice phase hydrometeors for WSM6 and WSM7 is compared in Fig. 3. Reflectivity in WSM6 is led by graupel, whereas the hail species is dominant in WSM7 (Fig. 3c, e). Reflectivity for snow is similar, but with a weakened magnitude along the leading edge after 4 h (Fig. 3a, b). The weakened magnitude for graupel in WSM7 than in
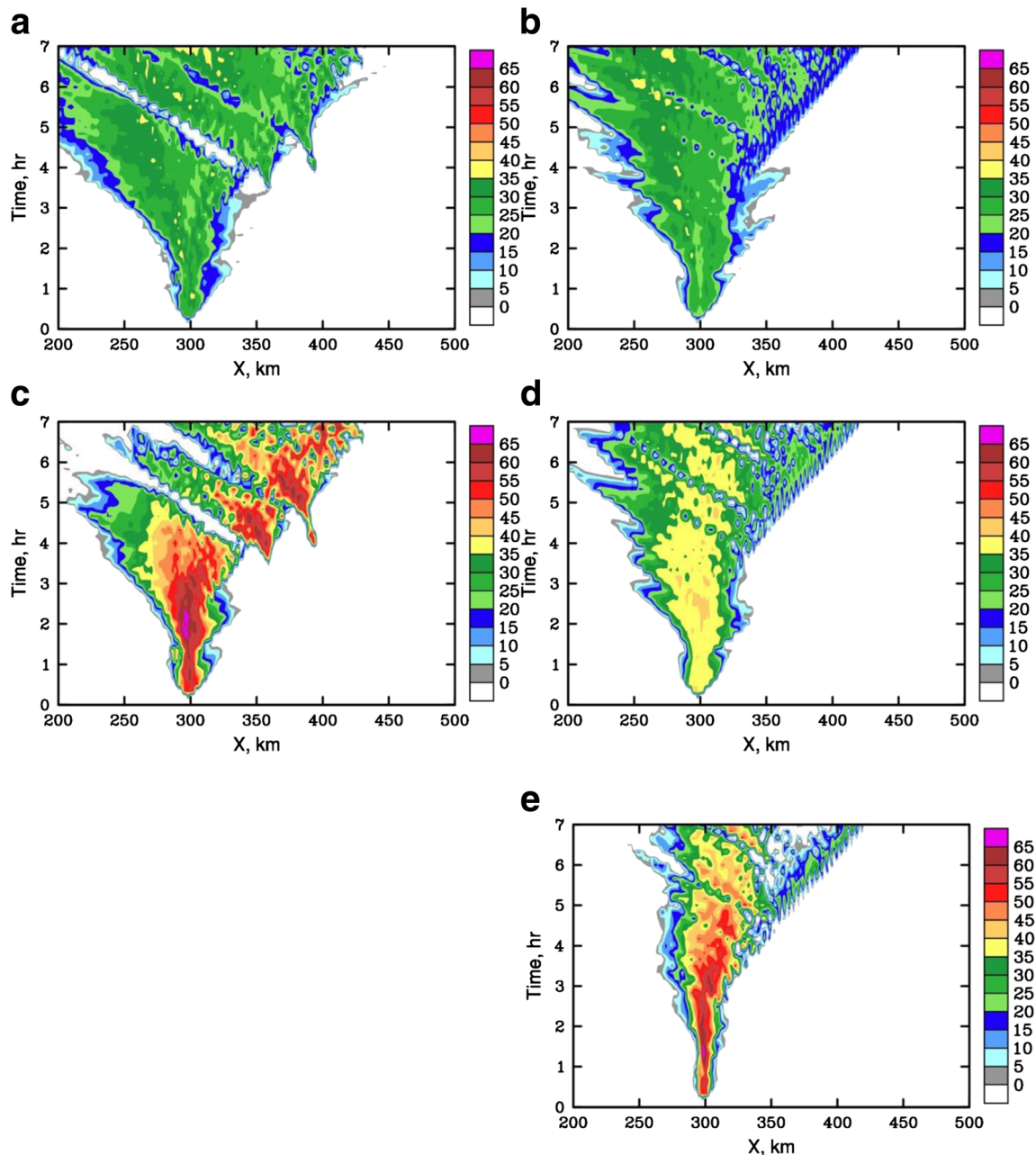

Fig. 3 Hovmöller plots of the maximum reflectivity of hydrometeors for WSM6 (left) and WSM7 (right). **a, b** snow; (**c, d**) graupel; (**e**) hail

WSM6 is largely compensated by hail (cf., Fig. 3c, d and e). It is seen that areas of maximum reflectivity for graupel broaden and become continuous in WSM7, whereas they are discontinuous in WSM6 (Fig. 3c, d). Evolutionary features of snow are also similar to that of graupel. Extended trailing snow in the stratiform cloud in WSM6, as compared to that in WSM7,

seems to be due to the fact that hail falls straight down, whereas graupel is transported backward into the stratiform region.

The vertical distributions of the domain-averaged water species for WSM6 and WSM7 are compared in Fig. 4a, b. The differences in the mixing ratios of the hydrometeors as a result of the hail processes are as follows. 1) Graupel

Fig. 4 Mixing ratio of hydrometeors (**a**, **b**) and process rate (**c**, **f**) for WSM6 (left column) and WSM7 (right column), which was time-domain- averaged for 0 h and 4 h and 280 km and 350 km. Pxacy is the process rate of the accretion of y by x hydrometeor (w = cloud water, r = rain, i = cloud ice, s = snow, g = graupel, and a: snow and graupel), Psaut is the process rate of the autoconversion of cloud ice to snow, Pigen is the process rate of the generation of cloud ice from water vapor, Pcond is the condensational/evaporational rate of cloud water, and Pxmlt is the process rate of the melting of x hydrometeor
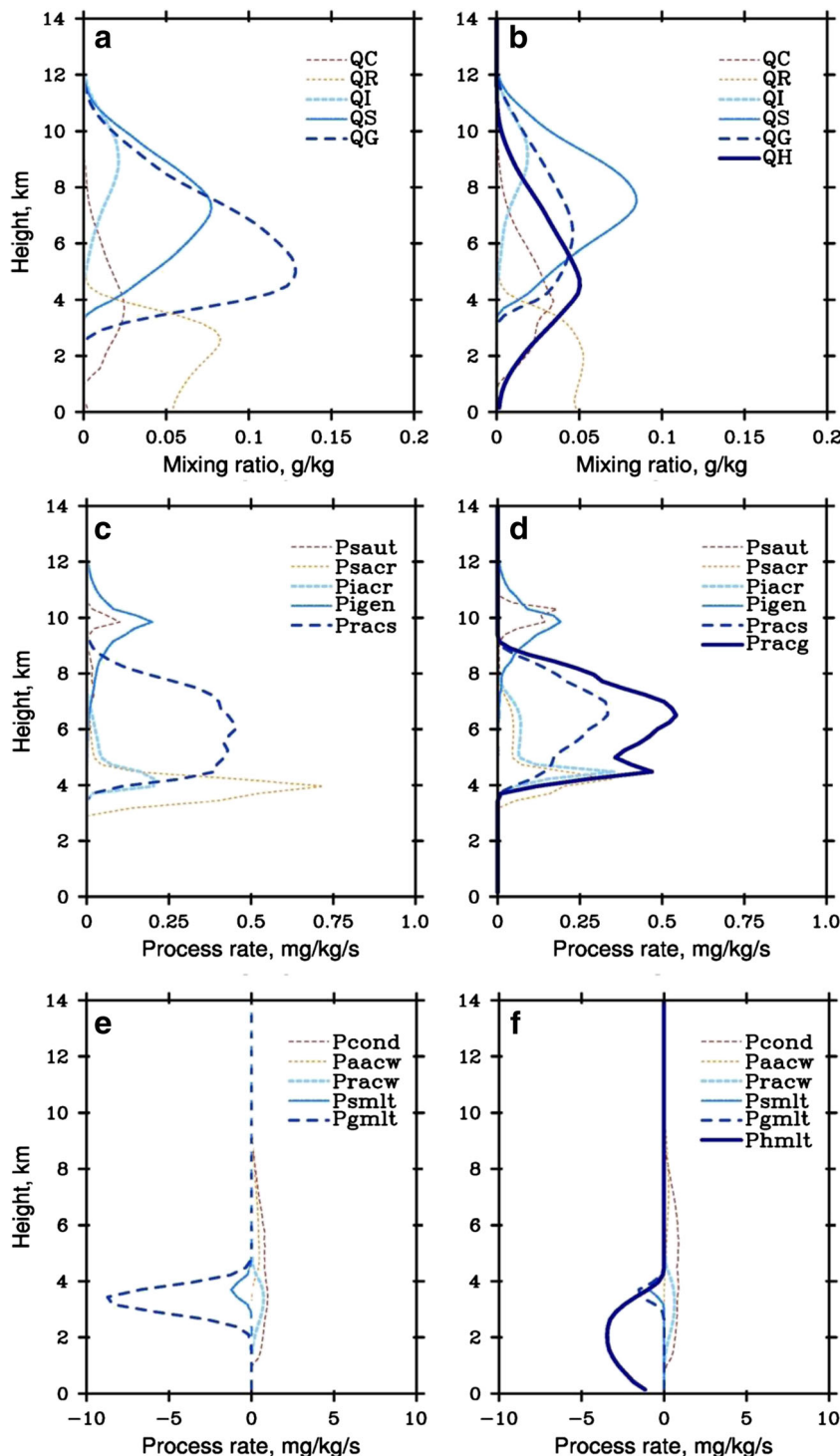
decreases by added hail and hail descends to the surface. 2) The snow and cloud ice between the two simulations do not make much difference. 3) The maximum mixing ratio of rain is at 3 km and rain in WSM7 is smaller than that in WSM6 below 4 km.

The process rates of the microphysical process and mixing ratios are compared for the WSM6 and WSM7 simulations (Fig. 4c, d, e and f). Six main processes are selected from among the cold (Fig. 4c, d) and warm processes (Fig. 4e, f). For the cold processes, in WSM6, the main processes are the accretion between snow and rain below 8 km and ice generation at around 10 km (Fig. 4c). Cloud ice is generated at 9–12 km and becomes snow by its aggregation. The generation of cloud ice from vapor and the aggregation of the cloud ice to snow are the main processes at 9–12 km. The process rate of the generation of cloud ice is higher than that of the aggregation of cloud ice. Snow becomes larger by the accretion of cloud water by snow, and the snow is converted to graupel by the accretion between rain and snow at the altitude of 4–8 km (Fig. 4c). In WSM7, those processes are accretion of graupel and snow by rain below 8 km and snow autoconversion increases at 10 km (Fig. 4d). As in WSM6, cloud ice and snow form in WSM7. Snow is converted not only to graupel but also to hail and graupel is converted to hail. The decreased graupel in WSM7 leads to slower descent and less aggregation with cloud water. Therefore, the graupel in WSM7 is smaller than that in WSM6.

For the warm processes, the primary process in WSM6 is the melting of graupel, whereas in WSM7, it is the melting of hail (Fig. 4e, f). The melting rate of graupel in WSM6 is larger than that of hail in WSM7. The amount of rain at the melting level depends on the amount of graupel and hail. The amount of graupel in WSM6 is larger than the sum of graupel and hail in WSM7, so the larger amount of graupel in WSM6 leads to a larger amount of rain at 2–4 km that in WSM7 (Fig. 4a, b and e, f). Therefore, there is less rain in WSM7 than in WSM6.

Figure 5 shows the probability density functions (PDFs) of precipitation in WSM6 and WSM7 between 0 and 4 h. The frequency of precipitation in WSM7 is increased except at the sections of 1–2 mm/10 min and 8–10 mm/10 min, compared to that in WSM6 (Fig. 5 top). The increase of light precipitation is due to descending hail and its subsequent melting process below a height of 3 km as shown in Fig. 4f. Heavy precipitation in WSM7 is increased due to the higher density of hail (Hong et al. 2010). In the 3D squall line experiments, along with the results of the 2D experiments, WSM7 tends to enhance heavy rainfall (> 12 mm/h) but suppress light and moderate precipitation (< 12 mm/h).
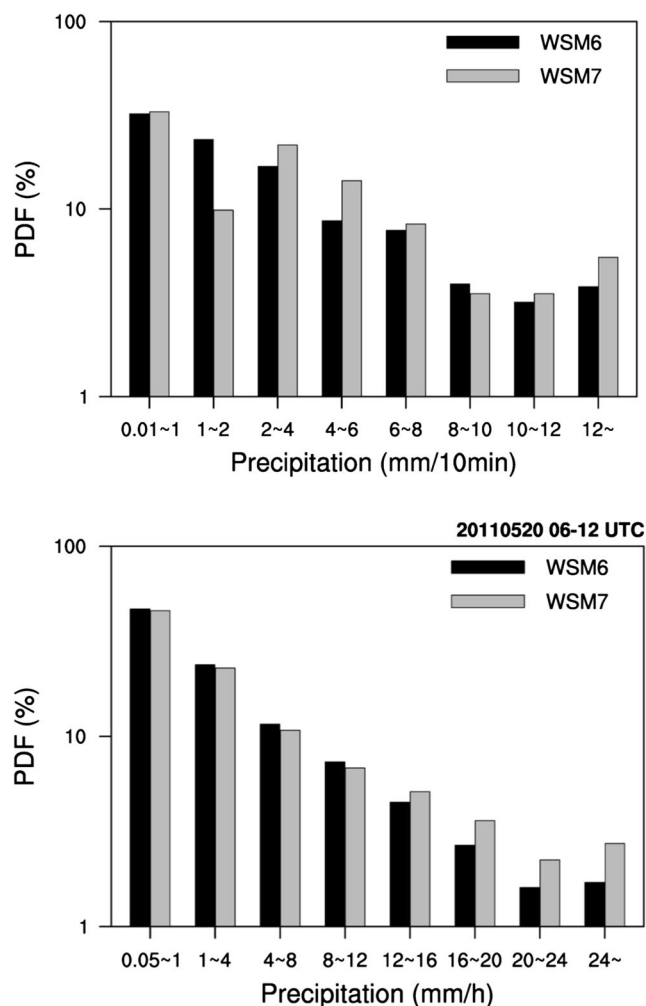

Fig. 5 PDFs of (top) the 10-min accumulated rainfall intensity for idealized squall line case experiments for 0 and 4 h and (bottom) 1-h accumulated rainfall for 06–12 UTC on 20 May 2011 MSE case for WSM6 (black) and WSM7 (gray) experiments

3.2 Real Case Simulations

Figure 6 shows horizontal cross-sections of the observed and simulated precipitation and the composite radar echoes at 10 UTC on 20 May 2011. The observation figures are from Tao et al. (2016). The precipitation in Fig. 6a is measured using the National Mosaic and Multi-sensor Quantitative Precipitation Estimates System (NMQ Q2). The observed reflectivity is from Next Generation Weather Radar (NEXRAD) data (Fig. 6d).

The NMQ Q2 data exhibit a well-developed squall line with an intense and slightly embowed convective leading edge (Fig. 6a). A trailing stratiform region is separated by a distinct transition region, which extends southwestward from the Kansas-Oklahoma border into central West Texas. The system is well organized on the mesoscale and its convective line is long and
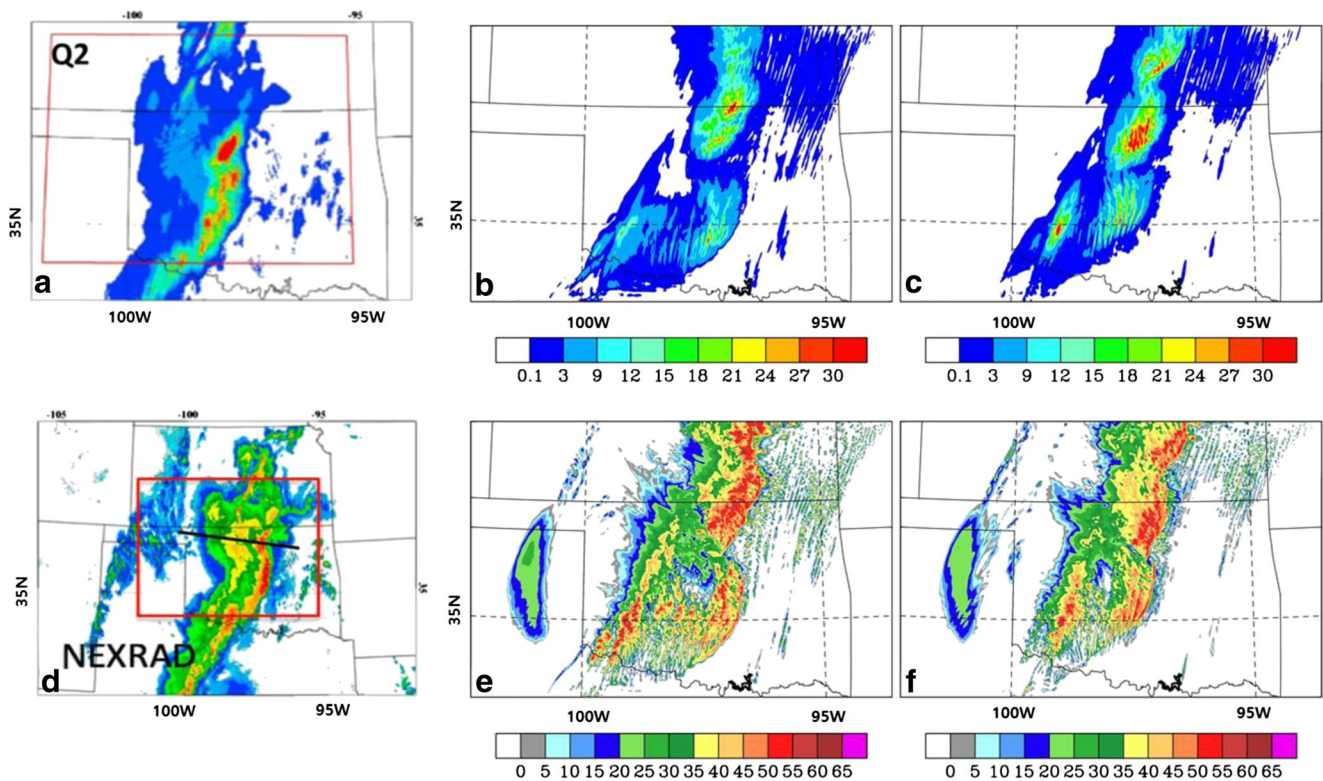
Fig. 6 1-h accumulated precipitation (top) and maximum reflectivity (bottom) for observation (**a**, **d**), WSM6 (**b**, **e**), and WSM7 (**c**, **f**) at 10 UTC on 20 May 2011. The observation figures are obtained from Tao et al. (2016)

consistent with a fairly uniform intensity and a bow shape. The trailing stratiform region is sizeable and expands continuously along the length of the line (Lang et al. 2014; Tao et al. 2016).

The precipitation of WSM6 and WSM7 shows embowed convective line from Kansas to southwest Oklahoma and a light precipitation area in southeastern Kansas (Fig. 6b, c). The WSM6 scheme produces a broad area of rain and weaker rain intensity in the convective leading edge than observation (Fig. 6b). The area of maximum precipitation is located at the Kansas-Oklahoma border and is at a northwestern position compared to observation. The area with precipitation <0.1 mm/h exists in the trailing stratiform region. Compared to WSM6 (Fig. 6c), the precipitation intensity in WSM7 is stronger, and the overall convective leading edge is more organized. Precipitation is concentrated in the convective squall line in northern Oklahoma and continues to south-central Oklahoma. The area of precipitation becomes narrower compared to that in WSM6 at the front of the convective leading edge, which is in southeastern Kansas and south-central Oklahoma. Another core of precipitation appears around southwestern Oklahoma (35°N, 99°W) and has strengthened compared with that of WSM6. The difference in vertical distribution of the hydrometeors between WSM6 and WSM7 is similar with that of the 2D results (not shown). Although rain decreases in WSM7 compared to WSM6, hail falling to the surface increases. Because of this, WSM7 tends to enhance

heavy rainfall (> 12 mm/h) but suppress light and moderate precipitation (< 12 mm/h) compared to WSM6 (Fig. 5 bottom).

The NEXRAD data show a similar trend with precipitation. The characteristics of precipitation are clearly seen in the evolution of reflectivity (Fig. 6d, e and f). The strong reflectivity (> 50, red color series) is located in the convective line and around southwestern Oklahoma. The line of strong reflectivity in WSM6 is broad and has a discontinuous bow shape (Fig. 6e). The moderate reflectivity (35 < reflectivity < 45, yellow color series) in WSM6 is located in the stratiform region (Kansas–northern Oklahoma) and is narrow. Compared to WSM6 (Fig. 6f), the strong reflectivity area in WSM7 becomes narrow and the line continues in a southward direction. The area with strong reflectivity in WSM6 generally has precipitation <15 mm/h, whereas that in WSM7 has precipitation of about 27 mm/h (Fig. 6b, c and e, f). This shows that the interrelations of intensity between precipitation and reflectivity are higher in WSM7 than in WSM6. This is caused by the difference of major hydrometeors between reflectivity and precipitation. Strong reflectivity in WSM6 is dominated by graupel, whereas hail and rain species are dominant in WSM7 (not shown). The precipitation in WSM6 comes as rain, but it comes as rain and hail in WSM7.

4 Summary and Conclusions

The effect of hail processes on simulated precipitation is examined. A four-ice scheme is developed by adding prognostic hail to the three-ice WSM6 scheme that has been widely used in mesoscale/cloud-resolving simulations. This new scheme, referred to as the WSM7 scheme, is implemented in the WRF model and tested with an idealized 2D thunderstorm testbed. Sensitivity simulations are performed to analyze the effect of hail on microphysical processes and precipitation.

As demonstrated in the idealized 2D framework, the WSM7 and WSM6 simulations exhibit comparable evolution of surface precipitation in squall lines. The overall evolution of the squall lines is similar in both cases, but the area of the trailing stratiform region is wider, and the rainfall intensity is strengthened when the hail category is included. The immediate effect of hail over graupel is enhanced accretion because of the more rapid sedimentation velocity and greater density of hail. The decreased intercept and slope parameters in WSM6 effectively increase the hydrometeor diameter, which results in faster sedimentation.

Hail with higher sedimentation velocity than graupel, falls more rapidly to the surface. Light rain increases due to hail below a height of 3 km, reducing the sum of graupel and hail compared to graupel simulated with the three-ice scheme. Because of the larger hail, heavy rain also increases, and the rain is well-organized in the convective squall line. The area of the stratiform region decreases due to the reduced sedimentation velocity of graupel. Hail is important to the production of intense echoes and heavy precipitation. The computational burden introduced by adding hail is increased by about 10% compared to that of WSM6.

We plan to perform additional analyses to understand the mechanisms underlying real world case studies better and to compare WSM7 with other microphysics schemes that include hail processes (e.g., the Goddard 4 ice scheme, WDM7).

Appendix

Microphysical processes to predict the mixing ratio and number concentration in WSM7

a. Production term for hail

(i) If the temperature is below 0 °C ($T < T_0$):

$$S_H = Phdep + Phaut + Pracg(1-\delta_2) + Pgacr(1-\delta_2) \\ + Phacw + Phacr + Phaci + Phacs + Phacg \tag{6}$$

where,

$$\delta_2 = \begin{cases} 1 & for\ q_R\ and\ q_S\ <\ 10^{-4}\ kg\ kg^{-1} \\ 0 & otherwise \end{cases}$$

(ii) If the temperature is above 0 °C ($T \geq T_0$):

$$S_H = Phacs + Phacg + Phevp + Pheml - Phmlt \tag{7}$$

1) ACCRETION (Phacw, Phacr, Phaci, Phacs, Phacg, Pracg)

Hail grows by accretion of other species, i.e., cloud water, cloud ice, rain, snow, and graupel. The collection of cloud water by hail is assumed to follow the continuous collection equation.

$$Phacw = \int_0^\infty \frac{1}{\rho} \frac{dM(D_H)}{dt} dD_H = \int_0^\infty \frac{1}{\rho} \frac{\pi}{4} \rho D_H^2 V_H(D_H) q_C E_{HC} n_{0H} \exp(-\lambda_H D_H) dD_H$$
$$= \frac{\pi a_H E_{HC} n_{0H} q_c}{4} \left(\frac{\rho_0}{\rho}\right)^{1/2} \frac{\Gamma(3+b_H)}{\lambda_H^{3+b_H}} \tag{8}$$

The accretion of rain, snow, and graupel by hail is assumed to follow the continuous collection equation:

$$\int_0^\infty \frac{1}{\rho} \frac{dM(D_H)}{dt} dD_H\ (kg\ kg^{-1}\ s^{-1})$$
$$= \int_0^\infty \pi \left(\frac{D_H + D_X}{2}\right)^2 |V_H - V_X| q_X E_{HX} n_H(D_H) dD_H \tag{9}$$
$$= \int_0^\infty \int_0^\infty \pi \left(\frac{D_H + D_X}{2}\right)^2 |V_H - V_X| \frac{\pi}{6} \rho_X D_X^3 n_X(D_X) E_{HX} n_H(D_H) dD_H$$

where the index $X \in [R, S, G]$ in Eq. (9) represents rain, snow, or graupel. Here, $n_R(D_R)$, $n_S(D_S)$, and $n_G(D_G)$ are exponential size distributions as follows.

$$n_R(D_R) = n_{0R} exp(-\lambda_R D_R) \tag{10}$$
$$n_S(D_S) = n_{0S} exp(-\lambda_S D_S) \tag{11}$$
$$n_G(D_S) = n_{0G} exp(-\lambda_G D_G) \tag{12}$$

Assuming negligible difference in sedimentation velocity for hail and rain with respect to the diameter of hail, we obtain the following accretion term of rain by hail

$$Phacr\ (kg\ kg^{-1}\ s^{-1}) \tag{13}$$
$$= \pi^2 E_{HR} n_{0R} n_{0H} |V_H - V_R| \frac{\rho_w}{\rho} \left(\frac{5}{\lambda_R^6 \lambda_H^1} + \frac{2}{\lambda_R^5 \lambda_H^2} + \frac{0.5}{\lambda_R^4 \lambda_H^3}\right).$$

Similarly, the accretions of snow (Phacs) and graupel (Phacg) by hail have the following form:

$$Phacs\ (kg\ kg^{-1}\ s^{-1})$$
$$= \pi^2 E_{HS} n_{0S} n_{0H} |V_H - V_S| \frac{\rho_S}{\rho} \left(\frac{5}{\lambda_S^6 \lambda_H^1} + \frac{2}{\lambda_S^5 \lambda_H^2} + \frac{0.5}{\lambda_S^4 \lambda_H^3}\right) \tag{14}$$

$Phacg\ (kg\ kg^{-1}\ s^{-1})$ $\qquad\qquad\qquad\qquad\qquad$ (15)

$$= \pi^2 E_{HG} n_{0G} n_{0H} |V_H - V_G| \frac{\rho_G}{\rho} \left(\frac{5}{\lambda_G^6 \lambda_H^1} + \frac{2}{\lambda_G^5 \lambda_H^2} + \frac{0.5}{\lambda_G^4 \lambda_H^3} \right).$$

The accretion of cloud ice by hail is also assumed to follow the continuous collection equation:

$$\int_0^\infty \frac{1}{\rho} \frac{dM(D_H)}{dt} dD_H \ (kg\ kg^{-1}\ s^{-1})$$

$$= \int_0^\infty \pi \left(\frac{D_H + D_I}{2} \right)^2 |V_H - V_I| q_I E_{HI} n_H(D_H) dD_H \qquad (16)$$

$$= \frac{\pi E_{HI} n_{0H} q_I}{4} |V_H - V_I| \left(\frac{2}{\lambda_H^3} + \frac{2D_I}{\lambda_H^2} + \frac{D_I^2}{\lambda_H} \right).$$

Hail production by the accretion of graupel of rain is obtained as Eq. (9) instead of

$Pracg\ (kg\ kg^{-1}\ s^{-1})$

$$= \pi^2 E_{GR} N_R n_{0G} |V_R - V_G| \frac{\rho_G}{\rho} \left(\frac{5}{\lambda_G^6} + \frac{4}{\lambda_G^5 \lambda_R^1} + \frac{1.5}{\lambda_G^4 \lambda_R^2} \right). \ (17)$$

Hail is assumed to grow by accretion by cloud ice, snow, and graupel if hail is wet when Phacr + Phacw ≥ 0.95Phwet. The wet growth of hail (Phwet) is computed using the formula for hail wet growth from Lin et al. (1983).

2) AGGREGATION (Phaut)

The autoconversion (aggregation) rate of graupel to hail is given by

$Phaut\ (kg\ kg^{-1}\ s^{-1})$

$$= max[10^{-3} \exp(0.09(T - T_0)\ (q_H - q_{S0})), 0], \qquad (18)$$

which occurs only for $T < T_0$.

3) DEPOSITION/SUBLIMATION (Phdep)

Sublimation/deposition will occur in a subsaturated and saturated regions as $S_I - 1 < 0$ and $S_I - 1 > 0$, respectively.

Here, S_I is the saturation ratio over ice. The continuous growth equation for hail if $T < T_0$ is given by

$Phdep\ (kg\ kg^{-1}\ s^{-1})$

$$= \frac{2\pi n_{0H}(S_I - 1)}{\rho(A_I + B_I)} \left[\frac{0.78\Gamma(2)}{\lambda_H^2} + 0.31 Sc^{1/3} \left(\frac{\rho_0}{\rho} \right)^{1/4} \left(\frac{a_H \rho}{\mu} \right)^{1/2} \frac{\Gamma\left(\frac{5 + b_H}{2} \right)}{\lambda_H^{\frac{5 + b_H}{2}}} \right],$$

$$\qquad\qquad\qquad\qquad\qquad\qquad\qquad\qquad\qquad\qquad (19)$$

where $A_I = \left(\frac{L_S}{K_a T} \right) \left(\frac{L_S}{K_a T} \right)$ and $B_I = \frac{R^* T}{D_f M_w e_{si}}$.

4) EVAPORATION (Phevp)

The evaporation based on Rutledge and Hobbs (1983), if $T \geq T_0$ is expressed as

$$Phevp\ (kg\ kg^{-1}\ s^{-1}) = \frac{2\pi n_{0H}(S_W - 1)}{\rho(A_W + B_W)} \qquad (20)$$

$$\left[\frac{0.78\Gamma(2)}{\lambda_H^2} + 0.31 Sc^{1/3} \left(\frac{\rho_0}{\rho} \right)^{1/4} \left(\frac{a_H \rho}{\mu} \right)^{1/2} \frac{\Gamma\left(\frac{5 + b_H}{2} \right)}{\lambda_H^{\frac{5 + b_H}{2}}} \right].$$

5) MELTING (Phmlt, Pheml)

The hail melted per unit time is given by

$$\frac{dM(D_H)}{dt} = -\frac{2\pi}{L_f} K_a D_H (T - T_0) F, \qquad (21)$$

where K_a is the thermal conductivity in J m^{-1} s^{-1} K^{-1}, and F is the ventilation factor. By multiplying the size distribution and integrating over all snow sizes to Eq. (21), we obtain the melting of hail if $T \geq T_0$, which is expressed as

$Phmlt\ (kg\ kg^{-1}\ s^{-1})$ $\qquad\qquad\qquad\qquad\qquad\qquad$ (22)

$$= -\frac{2\pi n_{0H} K_a (T - T_0)}{\rho L_f} \left(\frac{0.78}{\lambda_H^2} + 0.31 Sc^{\frac{1}{3}} \left(\frac{\rho_0}{\rho} \right)^{\frac{1}{4}} \left(\frac{a_H \rho}{\mu} \right)^{\frac{1}{2}} \frac{\Gamma\left(\frac{5 + b_H}{2} \right)}{\lambda_H^{\frac{5 + b_H}{2}}} \right).$$

The melting of hail is enhanced by the accretion of cloud water and rain, if $T \geq T_0$, and is expressed as

$Pheml\ (kg\ kg^{-1}\ s^{-1})$

$$= -\frac{C_w(T - T_0)}{L_f}(Phacw + Phacr). \qquad (23)$$

Table 2 List of symbols

Symbol	Description	Value	SI unit
A_I	Thermodynamic term	$\left(\frac{L_S}{K_aT}\right)\left(\frac{L_S}{R_vT}\right)$	m s kg^{-1}
A_W	Thermodynamic term	$\left(\frac{L_S}{K_aT}\right)\left(\frac{L_S}{R_vT}\right)$	m s kg^{-1}
a_G	Empirical formula of V_G	330	m^{1-b} s^{-1}
a_H	Empirical formula of V_H	285	m^{1-b} s^{-1}
a_R	Empirical formula of V_R	841.9	m^{1-b} s^{-1}
a_S	Empirical formula of V_S	11.72	m^{1-b} s^{-1}
B_I	Thermodynamic term	$\frac{R^*T}{D_f M_w e_{si}}$	m s kg^{-1}
B_W	Thermodynamic term	$\frac{R^*T}{D_f M_w e_{sw}}$	m s kg^{-1}
b_G	Empirical formula of V_G	0.8	
b_H	Empirical formula of V_H	0.8	
b_R	Empirical formula of V_R	0.8	
b_S	Empirical formula of V_S	0.41	
C_W	Specific heat of liquid water	4190	J kg^{-1} K^{-1}
D_C	Cloud water diameter		m
D_G	Graupel diameter		m
D_H	Hail diameter		m
D_I	Cloud ice diameter		m
D_R	Raindrop diameter		m
D_S	Snow diameter		m
D_X	Hydrometeor X diameter		m
E_{GR}	Graupel-rain collection efficiency	1	
E_{HC}	Hail-cloud water collection efficiency	1	
E_{HG}	Hail-graupel collection efficiency	0.5	
E_{HI}	Hail-cloud ice collection efficiency	$\exp[0.07(T - T_0)]$	
E_{HR}	Hail-rain collection efficiency	1	
E_{HS}	Hail-snow collection efficiency	1	
E_{HX}	Hail-hydrometeor X collection efficiency		
e_{si}	Saturation vapor pressure for ice		kg m^{-1} s^{-2}
e_{si}	Saturation vapor pressure for water		kg m^{-1} s^{-2}
F	Ventilation factor	$0.78 + 0.31\mathrm{Sc}^{1/3}\mathrm{Re}^{1/2}$	
K_a	Thermal conductivity of air	2.43×10^{-2}	J m^{-1} s^{-1} K^{-1}
L_f	Latent heat of fusion	3.34×10^5	J kg^{-1}
L_S	Latent heat of sublimation	2.5×10^6	J kg^{-1}
L_V	Latent heat of condensation	2.5×10^6	J kg^{-1}
M_W	Molecular weight of water	18.0160	kg kmol^{-1}
N_C	Number concentration of cloud water	3×10^8	m^{-3}
N_H	Number concentration of hail		m^{-3}
N_R	Number concentration of rain		m^{-3}
$n_G(D_G)$	Number concentration of graupel of diameter D_G		m^{-4}
$n_H(D_H)$	Number concentration of hail of diameter D_H		m^{-4}
$n_R(D_R)$	Number concentration of rain of diameter D_R		m^{-4}
$n_S(D_S)$	Number concentration of snow of diameter D_S		m^{-4}
$n_X(D_X)$	Number concentration of hydrometeor of diameter D_X		m^{-4}
n_{0G}	Intercept parameter of graupel	4×10^6	m^{-4}
n_{0H}	Intercept parameter of hail	4×10^4	m^{-4}
n_{0R}	Intercept parameter of rain	8×10^6	m^{-4}
n_{0S}	Intercept parameter of snow	$2 \times 10^6 \exp[0.12(T - T_0)]$	m^{-4}
Paacw	Production rate for accretion of cloud water by snow and graupel		kg kg^{-1} s^{-1}
Pcond	Production rate for condensational/evaporational rate of cloud water		kg kg^{-1} s^{-1}
Pgacr	Production rate for accretion of rain by graupel		kg kg^{-1} s^{-1}
Pgacg	Production rate for accretion of graupel by hail		kg kg^{-1} s^{-1}
Pgmlt	Production rate for instantaneous melting of graupel		kg kg^{-1} s^{-1}
Phacg	Production rate for accretion of graupel by hail		kg kg^{-1} s^{-1}
Phaci	Production rate for accretion of cloud ice by hail		kg kg^{-1} s^{-1}
Phacr	Production rate for accretion of rain by hail		kg kg^{-1} s^{-1}
Phacs	Production rate for accretion of snow by hail		kg kg^{-1} s^{-1}
Phacw	Production rate for accretion of cloud water by hail		kg kg^{-1} s^{-1}
Phaut	Production rate for autoconversion of graupel to form hail		kg kg^{-1} s^{-1}
Phdep	Production rate for deposition/sublimation rate of graupel		kg kg^{-1} s^{-1}
Pheml	Production rate induced by enhanced melting rate of hail		kg kg^{-1} s^{-1}
Phevp	Production rate for evaporation of melting hail		kg kg^{-1} s^{-1}
Phmlt	Production rate for instantaneous melting of hail		kg kg^{-1} s^{-1}
Phwet	Wet growth of hail		kg kg^{-1} s^{-1}
Piacr	Production rate for accretion of rain by cloud ice		kg kg^{-1} s^{-1}
Pigen	Production rate for generation of ice from water vapor		kg kg^{-1} s^{-1}

Table 2 (continued)

Symbol	Description	Value	SI unit
$Pracg$	Production rate for accretion of graupel by rain		kg kg^{-1} s^{-1}
$Pracs$	Production rate for accretion of snow by rain		kg kg^{-1} s^{-1}
$Pracw$	Production rate for accretion of cloud water by rain		kg kg^{-1} s^{-1}
$Psacr$	Production rate for accretion of rain by snow		kg kg^{-1} s^{-1}
$Psaut$	Production rate for autoconversion of cloud ice to form snow		kg kg^{-1} s^{-1}
$Psmlt$	Production rate for instantaneous melting of snow		kg kg^{-1} s^{-1}
q_C	Mixing ratio of cloud water		kg kg^{-1}
q_G	Mixing ratio of graupel		kg kg^{-1}
q_H	Mixing ratio of hail		kg kg^{-1}
q_I	Mixing ratio of cloud ice		kg kg^{-1}
q_S	Mixing ratio of snow		kg kg^{-1}
q_{S0}	Threshold amount for aggregation to occur	6×10^{-4}	kg kg^{-1}
q_X	Mixing ratio of hydrometeor X		kg kg^{-1}
R^*	Universal gas constant	8.314×10^3	J mol^{-1} K^{-1}
Sc	Schmidt number	0.6	
S_I	Saturation ratio over ice		
S_W	Saturation ratio with respect to water		
T	Temperature		K
T_0	Reference temperature	273.16	K
V_G	Mass-weighted fall speed of graupel		m s^{-1}
V_H	Mass-weighted fall speed of hail		m s^{-1}
V_I	Mass-weighted fall speed of cloud ice		m s^{-1}
V_R	Mass-weighted fall speed of rain		m s^{-1}
V_S	Mass-weighted fall speed of snow		m s^{-1}
V_X	Mass-weighted fall speed of hydrometeor X		m s^{-1}
$V_H(D_H)$	Fall speed of hail of diameter D_H		m s^{-1}
Γ	Complete gamma function		
λ_G	Slope of graupel size distribution		m^{-1}
λ_H	Slope of hail size distribution		m^{-1}
λ_R	Slope of rain size distribution		m^{-1}
λ_S	Slope of snow size distribution		m^{-1}
δ_2	Hail-graupel collection efficiency		
μ	Dynamic viscosity of air	1.718×10^{-5}	g m^{-1} s^{-1}
ρ	Density of air		kg m^{-3}
ρ_G	Density of graupel	500	kg m^{-3}
ρ_H	Density of hail	912	kg m^{-3}
ρ_S	Density of snow	100	kg m^{-3}
ρ_W	Density of water	1000	kg m^{-3}
ρ_X	Density of hydrometeor X		kg m^{-3}
ρ_0	Density of air at reference state	1.28	kg m^{-3}

References

Chou, M.-D., and M. J. Suarez, 1999 A shortwave radiation parameterization for atmospheric studies. NASA/TM-1999-104606, **15**, pp 40

Chou, M.-D., and M. J. Suarez, 2001 A thermal infrared radiation parameterization for atmospheric studies. NASA/TM-2001-104606, **19**, pp593

Colle, B.A., Zeng, Y.: Bulk microphysical sensitivities within the MM5 for orographic precipitation. Part I: the sierra 1986 event. Mon. Weather Rev. **132**, 2780–2801 (2004)

Dudhia, J., Hong, S.-Y., Lim, K.-S.: A new method for representing mixed-phase particle fall speeds in bulk microphysics parameterizations. J. Meteorol. Soc. Japan. **86A**, 33–44 (2008)

Grasso, L., Lindsey, D.T., Lim, K.-S.S., Clark, A., Bikos, D., Dembek, S.R.: Evaluation of and suggested improvements to the WSM6 microphysics in WRF-ARW using synthetic and observed GOES-13 imagery. Mon. Wea. Rev. **142**, 3635–3650 (2014). https://doi.org/10.1175/MWR-D-14-00005.1

Grell, G.A., Devenyi, D.: A generalized approach to parameterizing convection combining ensemble and data assimilation techniques. Geophys. Res. Lett. **29**, 1693–38-4 (2002). https://doi.org/10.1029/2002GL015311

Han, M., Braun, S.A., Matsui, T., Williams, C.R.: Evaluation of cloud microphysics schemes in simulations of a winter storm using radar and radiometer measurements. J. Geophys. Res. **118**, 1401–1419 (2013). https://doi.org/10.1002/jgrd.50115

Hong, S.-Y., Lim, J.-O.J.: The WRF single-moment 6-class microphysics scheme (WSM6). J. Kor. Meteorol. Soc. **42**, 129–151 (2006)

Hong, S.-Y., Dudhia, J., Chen, S.-H.: A revised approach to ice microphysical processes for the bulk parameterization of clouds and precipitation. Mon. Wea. Rev. **132**, 103–120 (2004)

Hong, S.-Y., Lim, K.-S.S., Lee, Y.H., Ha, J.C., Kim, H.W., Ham, S.J., Dudhia, J.: Evaluation of the WRF double-moment 6-class microphysics scheme for precipitation convection. Adv. Meteorol. **2010**, 1–10 (2010). https://doi.org/10.1155/2010/707253

Lang, S.E., Tao, W.-K., Chern, J.-D., Wu, D., Li, X.: Benefits of a fourth ice class in the simulated radar reflectivities of convective systems using a bulk microphysics scheme. J. Atmos. Sci. **71**, 3583–3612 (2014)

Li, X., Pu, Z.: Sensitivity of numerical simulation of early rapid intensification of hurricane Emily (2005) to cloud microphysical and planetary boundary layer parameterizations. Mon. Wea. Rev. **136**(136), 4819–1838 (2008)

Lim, J.-O. J. and S.-Y. Hong, 2005 Effects of bulk ice microphysics on the simulated monsoonal precipitation over East Asia. J. Geophys. Res., 110, D24201, https://doi.org/10.1029/2005JD006166.

Lim, K.-S.S., Hong, S.-Y.: Development of an effective double-moment cloud microphysics scheme with prognostic cloud condensation nuclei (CCN) for weather and climate models. Mon. Wea. Rev. **138**, 1587–1612 (2010)

Lin, Y., Colle, B.A.: The 4-5 December 2001 IMPROVE-2 event: observed microphysics and comparisons with the weather research and forecasting model. Mon. Wea. Rev. **127**, 1372–1392 (2009)

Lin, Y.-L., Farley, R.D., Orville, H.D.: Bulk parameterization of the snow field in a cloud model. J. Clim. Appl. Meteor. **22**, 1065–1092 (1983)

Locatelli, J.D., Hobbs, P.V.: Fallspeeds and masses of solid precipitation particles. J. Geophys. Res. **79**, 2185–2197 (1974)

Luo, L., Xue, M., Zhu, K. Zhou, B.: Explicit prediction of hail using multimoment microphysics schemes for a hailstorm of 19 March 2014 in eastern China. J. Geophys. Res. **122**, (2017). https://doi.org/10.1002/2017JD026747

Mellor, G.L., Yamada, T.: Development of a turbulence closure model for geophysical fluid problems. Rev. Geophys. Space Phys. **20**, 851–875 (1982)

Milbrandt, J.A., Morrison, H.: Prediction of graupel density in an bulk microphysics scheme. J. Atmos. Sci. **70**, 410–429 (2013)

Morrison, H., Curry, J.A., Khvorostyanov, V.I.: A new double-moment microphysics parameterization for application in cloud and climate models. Part I: description. J. Atmos. Sci. **62**, 1665–1677 (2005)

Morrison, H., Thompson, G., Tatarskii, V.: Impact of cloud microphysics on the development of trailing stratiform precipitation in a simulated squall line: comparison of one- and two-moment scheme. Mon. Wea. Rev. **137**, 991–1007 (2009)

Petersen, W.A., Jensen, M.: The NASA-GPM and DOE-ARM mid latitude continental convective clouds experiment (MC3E). Earth Observer. **24**, 12–18 (2012)

Rutledge, S.A., Hobbs, P.V.: The mesoscale and microscale structure and organization of clouds and precipitation in midlatitude cyclones. VIII: a model for the "seeder-feeder" process in warm-frontal rainbands. J. Atmos. Sci. **40**, 1185–1206 (1983)

Rutledge, S. A., Hobbs, P. V.: The mesoscale and microscale structure and organization of clouds and precipitation in midlatitude cyclones. XII: A diagnostic modeling study of precipitation development in narrow cold-frontal rainbands. J. Atmos. Sci. **41**, 2949–2972 (1984)

Shi, J. J., W.-K. Tao, S. Lang, S. S. Chen, S.-Y. Hong, and C. Peters-Lidard, 2007 An Improved Bulk Microphysical Scheme for Studying Precipitation Processes: Comparisons with Other Schemes. AGU Joint Assembly, Acapulco, Mexico, May 2007

Shin, H., Hong, S.-Y.: Quantitative precipitation forecast experiments of heavy rainfall over Jeju Island on 14-16 September 2007 using the WRF model. Asia-Pac. J. Atmos. Sci. **45**, 71–89 (2009)

Skamarock, W. C., et al., 2008 A description of the advanced research WRF version 3. NCAR tech. Note NCAR/TN-475+STR

Tao, W.-K., Wu, D., Lang, S., Chern, J.-D., Peters-Lidard, C., Fridlind, A., Matsui, T.: High-resolution NU-WRF simulations of a deep convective-precipitation system during MC3E: further improvements and comparisons between Goddard microphysics schemes and observations. J. Geophys. Res. **121**, 1278–1305 (2016)

Thompson, G., Field, P.R., Rasmussen, R.M., Hall, W.D.: Explicit forecasts of winter precipitation using an improved bulk microphysics scheme. Part II: implementation of a new snow parameterization. Mon. Wea. Rev. **136**, 5095–5155 (2008)

van Weverberg, K., van Lipzig, N.P., Delobbe, L., Vogelmann, A.M.: The role of precipitation size distributions in km-scale NWP simulations of intense precipitation: evaluation of cloud properties and surface precipitation. Q. J. R. Meteorol. Soc. **138**, 2163–2181 (2012). https://doi.org/10.1002/qj.1933

Wu, D., Dong, X., Xi, B., Feng, Z., Kennedy, A., Mullendore, G., Gilmore, M., Tao, W.-K.: Impacts of microphysical scheme on convective and stratiform characteristics in two high precipitation squall line events. J. Geophys. Res. **118**, 11119–11135 (2013)